RSC Advances

PAPER

View Article Online
View Journal | View Issue

Cite this: *RSC Adv.*, 2025, **15**, 19522

Phosphorus and boron enhanced N-doped carbon nanofibers for enhanced lithium ion storage

Yaqi Ren,[ac] Junchen Tian,[a] Sangwan Li,[a] Xi Li,[a] Xiangyuan Zhao,[ac] Xiang Wang,[a] Pengchong Yang,[a] Jiaming Ni,[a] Xixi Ji*[b] and Pingping Liu*[a]

Received 10th February 2025
Accepted 29th May 2025

DOI: 10.1039/d5ra00982k

rsc.li/rsc-advances

A phosphorus (P), and boron (B) enhanced N-doped carbon nanofiber materials was prepared *via* a facile electrospinning method as a binder-free anode for lithium-ion storage applications. The triple-doped binder-free electrode demonstrated a high specific capacity of 611.2 mA h g^{-1} at a current density of 0.1 A g^{-1} and a high capacity retention of 94.8% after 500 cycles. This work demonstrates that adding P and B in N-doped carbon materials can significantly improve electrochemical properties and provides a methodology for the development of carbon-based materials for energy storage applications.

Introduction

Lithium-ion batteries (LIBs) and lithium-ion capacitors (LICs) are recognized as promising energy storage technologies for applications in electric vehicles, portable electronic devices, and large-scale power grid storage, owing to the high energy density of LIBs, as well as the exceptional energy density, high power density, and long cycle life of LICs.[1,2] While LIBs and LICs fundamentally differ in their energy/power density trade-offs, their anode materials share similarities, often undergoing faradaic reactions wherein lithium ions are reversibly intercalated into or extracted from the battery-type anode during charge/discharge processes. This mechanism enables high energy density, low self-discharge rates, superior rate performance, and excellent cycling stability, collectively positioning them as a research focal point.[3,4] A wide range of anode materials, such as alloy-based materials,[5] metal–organic frameworks (MOFs),[6] and intercalation-type materials,[7] have been developed to advance LIB and LIC technology. Among them, disordered carbon-based materials have gained widespread attention as anode materials due to their outstanding properties, including high specific surface area (SSA), excellent chemical/electrochemical stability, and structural features such as amorphous frameworks, wide interlayer spacing, and abundant surface defects.[8,9] For instance, Bhattacharjee *et al.*[10] synthesized a porous and disordered carbon-rich polymer material for use as an anode in LICs, achieving an I_D/I_G ratio of 2.02 and demonstrating a specific capacity of 130 mA h g^{-1} at a current density of 1 A g^{-1} in half-cell configurations. Wang *et al.*[11] reported a lignin-derived nanosized honeycomb-like porous carbon materials, with a 483.8 mA h g^{-1} after 100 cycles at a current density of 100 mA g^{-1}.

Heteroatom doping has been extensively employed to enhance the chemical and electrochemical properties of carbon-based materials.[12] N-Doped carbon materials have found widespread applications, as the introduction of nitrogen atoms can significantly boost conductivity, expedite charge transfer, and augment the surface wettability of carbon materials.[13,14] However, nitrogen doping alone is often insufficient to markedly enhance the material's electrochemical performance, due to its limited capacity to optimize electronic conductivity and active site distribution.[15] To address this limitation, the incorporation of phosphorus (P) or boron (B) atoms has been proposed as an effective strategy to further modify N-doped carbon materials. Phosphorus doping or functionalization can create topological defects that exhibit higher electronic capabilities than carbon. This significantly accelerates the storage and transport kinetics of lithium ions (Li^+).[16] Boron doping, on the other hand, can enhance the adsorption strength between lithium and carbon atoms, which in turn leads to a substantial increase in lithium-ion storage capacity.[17] Additionally, nitrogen and phosphorus with rich electrons and boron with low electrons can provide more electroactive sites and improve the electron transfer rate in the electrochemical process.[18] Furthermore, the larger atomic size of phosphorus and boron than carbon can increase the interlayer spacing, thus enhancing the electrochemical properties and stability of carbon materials.[19] Thus, doping with P and B heteroatoms can synergistically enhance the material's surface properties, electronic structure, and catalytic activity, which makes them promising candidates for boosting the performance of N-doped carbon materials in LIBs and LICs.[16–19] Alomari *et al.*[20] prepared a 3D nitrogen and phosphorous co-doped reduced graphene aerogel *via* a hydrothermal method, which delivered a specific capacity

[a]*School of Materials and Environmental Engineering, Chengdu Technological University, Chengdu, 611730, China. E-mail: liupp5216@126.com*

[b]*College of Automobile and Mechanical Engineering, Changsha University of Science and Technology, Changsha 410114, China. E-mail: jixixi201408@163.com*

[c]*Sichuan Engineering Research Center for Small & Medium-sized Intelligent Sewage Treatment Equipment, Chengdu 611730, China*

of 120 mA h g^{-1} at 0.1 A g^{-1}. Yang *et al.*[19] prepared a N/P dual-doped carbon nanofiber film anode *via* an electrospinning process, which exhibited a high capacity of 507.3 mA h g^{-1} at 0.1 A g^{-1}. Significant research efforts have been devoted to single-element modified N-doped carbon materials, whereas studies on dual-element enhanced N-doped carbon materials for LICs applications remain relatively limited.[21]

In this study, we have successfully fabricated a binder-free, P,B-enhanced N-doped carbon nanofiber electrode *via* the electrospinning method for use as an anode in LICs. This innovative approach offers several distinct advantages. Firstly, the stable and binder-free carbon nanofiber network provides abundant channels for ion/electron transmission, eliminating the interference of insulating binders. Secondly, electrospinning ensures uniform doping of N, P, and B within the carbon nanofibers, maximizing the synergistic effects of these elements. Thirdly, the co-doping of P, and B creates numerous electroactive sites compared with N-doped carbon nanofibers, significantly enhancing the electrode's electrochemical performance compared to materials doped with a single element or a combination of two elements. The resulting electrode exhibits a high specific capacity of 611.2 mA h g^{-1} at 0.1 A g^{-1} and maintains a high capacity retention rate of 94.8% after 500 cycles. This work not only provides a new pathway for enhancing carbon-based materials for LICs but also holds great promise for applications in related fields.

Experimental

Materials preparation

A sol precursor was prepared by adding 0.6 g of polyacrylonitrile (PAN, M_w = 150 000, Aldrich), 0.2 mL of tributyl borate (TB, Aladdin), and 0.25 g of melamine polyphosphate (MP, Aladdin) to 10 mL *N*,*N*-dimethylformamide (DMF, Aladdin) and magnetic stirring for 12 h. Then the sol precursor were transferred to the injection pump for electrospinning. The electrospinning was developed at a fixed voltage of 16 kV, a pumping rate of 1.8 mL h^{-1}, and a fixed distance of 15 cm between the collection and the needle, and the fibers were collected by a piece of aluminum foil. The collected composite fibers were stripped from aluminum foil and transferred to a tube furnace, and heated at 250 °C for 3 h with a heating rate of 2 °C min^{-1} in air for stabilization, and then heated at 800 °C for 3 h with a heating rate of 2 °C min^{-1} in Ar atmosphere. The as-prepared material was named as CNF–N,P,B. For comparison, the materials with different types of the doping elements were named as CNF–N (only adding PAN), CNF–N,P (only adding PAN and MP), and CNF–N,B (only adding PAN and TB), respectively.

Materials Characterization

Scanning electron microscopy (SEM, Thermo Scientific Helios 5CX), transmission electron microscopy (TEM, JEOL JEM-F200), Raman spectrometer (Horiba Scientific LabRAM HR Evolution), and X-ray diffraction (XRD, Rigaku Ultima IV) were used to characterize the structures of the samples. Nitrogen adsorption isotherms were measured at 77 K by a 3H-2000PM2 analyzer to determine the specific surface area (SSA) of the samples. Before measurements, the samples were degassed in vacuum at 200 °C for 6 h. The SSA and pore sizes were computed by the Brunauer–Emmett–Teller (BET) method and the adsorption branches of the isotherms using the Barrett–Joyner–Halenda (BJH) model, respectively. X-ray photoelectron spectroscopy (XPS, ESLALAB 250Xi, USA) was used to detect the bonding states and composition of the samples.

Electrochemical Measurements

The electrochemical properties of the samples were tested using 2025-type coin cells. The samples were cut into round slices (14 mm in diameter), weighed accurately, (about 2–3 mg), and directly used as binder-free anodes. In a glovebox full of Ar, CNF–N, CNF–N,P, CNF–N,B, and CNF–N,P,B anodes were used to assemble LICs, and celgard 2500 films, Li foils, and 1 mol L^{-1} $LiPF_6$ in dimethyl carbonate/diethyl carbonate/ethylene carbonate (1 : 1 : 1 by volume) were used as membranes, counter electrode, and electrolyte, respectively.

Results and discussion

The structural characteristics of the samples were examined using SEM. Fig. 1a–d reveal that the samples exhibit smooth surfaces with continuous fibrous morphologies, indicative of a low presence of large pores. The average diameters of the CNF–N, CNF–N,P, CNF–N,B, and CNF–N,P,B fibers were measured to be 350 nm, 200 nm, 200 nm, and 150 nm, respectively, which indicating that the more doping elements there are, the smaller the diameter. This is because the carbon

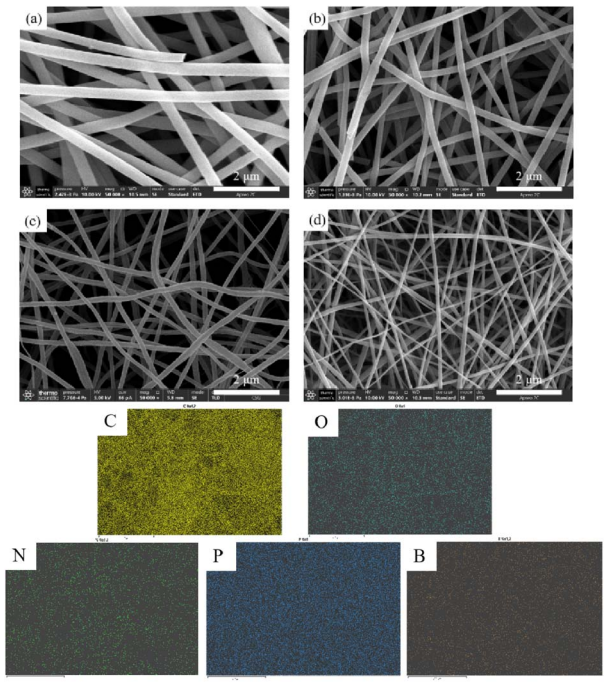

Fig. 1 SEM images of (a) CNF–N, (b) CNF–N,P, (c) CNF–N,B, (d) CNF–N,P,B and EDS mappings of C, O, N, P, and B for CNF–N,P,B.

skeleton is primarily derived from PAN, while TB and MB contribute only a small amount of doping elements. Thus, the proportion of PAN decreases with the addition of TB and/or MB, leading to a reduction in the diameters of CNFs-N,P and CNFs-N,B compared with CNFs-N, and the CNFs-N,P,B exhibits the smallest diameter. Additionally, the EDS elemental mapping of CNFs-N,P,B (Fig. 1e) shows uniform distributions of N, P, and B throughout the sample.

The TEM characterization of CNF–N,P,B is shown in Fig. 2, which reveals nanofibers with diameters ranging from 100 to 150 nm (Fig. 2a), demonstrating excellent consistency with the dimensions observed in the previously obtained SEM results. Meanwhile, TEM analysis reveals distinct mesoporous structures within the fiber matrix (Fig. 2a), a morphological feature we attribute to the thermally induced decomposition and volatilization of organic constituents (PAN, TB, and MP precursors) during calcination. This controlled elimination of volatile components creates interconnected pore networks while maintaining structural integrity. High-resolution TEM analysis (Fig. 2b) exhibits characteristic features of amorphous carbon materials, with no discernible lattice fringes present in the fibrous structures. This observation is further corroborated by the selected-area electron diffraction pattern (Fig. 2c), which displays diffuse diffraction rings devoid of sharp crystalline reflections, conclusively confirming the amorphous carbon configuration.

As shown in Fig. 3a, the X-ray diffraction (XRD) patterns exhibit a single broad peak at around 24°, corresponding to the (002) crystal planes in the amorphous carbon structure with a low degree of graphitization. The (002) peaks of CNFs-N, CNFs-N,P, CNFs-N,B, and CNFs-N,P,B are located at 24.72°, 24.04°, 24.16°, and 23.74°, respectively, indicating that the addition of P and B enhances the disorder of the carbon materials.[16] This conclusion is further supported by Raman spectroscopy results, as shown in Fig. 3b. The I_D/I_G ratio, a crucial indicator for assessing the degree of disorder in carbon materials, reflects the relative intensities of the D band (disordered carbon) and G band (ordered carbon).[22,23] The I_D/I_G ratios of CNFs-N, CNFs-N,P, CNFs-N,B, and CNFs-N,P,B are 1.01, 1.04, 1.02, and 1.08, respectively, indicating that P and B doping result in the generation of more defects.[24]

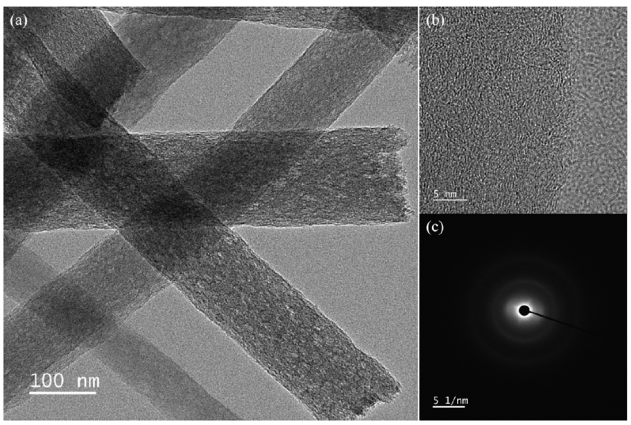

Fig. 2 (a) TEM image, (b) HRTEM analysis, (c) SAED of CNF-N,P,B.

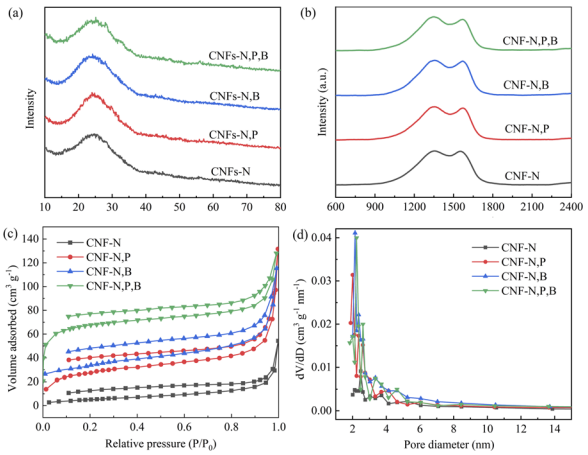

Fig. 3 (a) XRD patterns, (b) Raman spectra, (c) nitrogen adsorption–desorption isotherms, and (d) pore size distributions of different CNF samples.

Anode materials for LICs necessitate a large SSA to provide ample active sites for enhanced electrochemical performance. To this end, nitrogen adsorption/desorption isotherms were meticulously measured to scrutinize the SSA of the fabricated samples. As depicted in Fig. 2c, all samples exhibited a combination of type-I and type-IV isotherms, indicative of the presence of both micropores and mesopores.[25] The SSAs of CNF–N, CNF–N,P, CNF–N,B, and CNF–N,P,B were determined to be 20.49, 97.84, 116.88, and 252.00 $m^2\ g^{-1}$, respectively. Additionally, the average pore diameters of these samples were measured to be 12.22, 6.67, 5.87, and 3.12 nm, respectively. As shown by the SEM images in Fig. 1, the more types of dopants introduced, the smaller the fiber diameter, which in turn boosts SSA. Simultaneously, the SSA significantly increased and the pore sizes notably decreased following doping, suggesting that the introduction of P and B dopants facilitated the formation of more mesoporous and microporous structures. This enhanced SSA is anticipated to bolster the electrochemical properties of the doped materials.[26]

The N content of the samples were analyzed using XPS, with the results presented in Fig. 4. The XPS survey spectra of the samples reveal several peaks at 133.0, 191.0, and 400.0 eV, corresponding to P, B, and N, respectively. The N 1s spectra of the samples exhibit peaks at 398.3, 400.0, 401.2, and 405.0 eV, which are attributed to pyridinic nitrogen (N1), pyrrolic nitrogen (N2), graphitic-N (N3), and N–O bond (N4), respectively.[19] Pyridinic-N, pyrrolic-N, and N–O bond facilitate pseudocapacitive charge storage through redox-active sites, whereas graphitic-N improves electronic conductivity *via* electron donation to the carbon matrix.[27,28] It is evident that the incorporation of P and B leads to an increase in the content of pyridinic nitrogen, while the addition of B results in a higher content of pyrrolic nitrogen. Besides, there is a positive correlation between heteroatom co-doping concentration and N–O bond content, suggesting synergistic chemical interactions during the pyrolysis process. The nitrogen contents in the

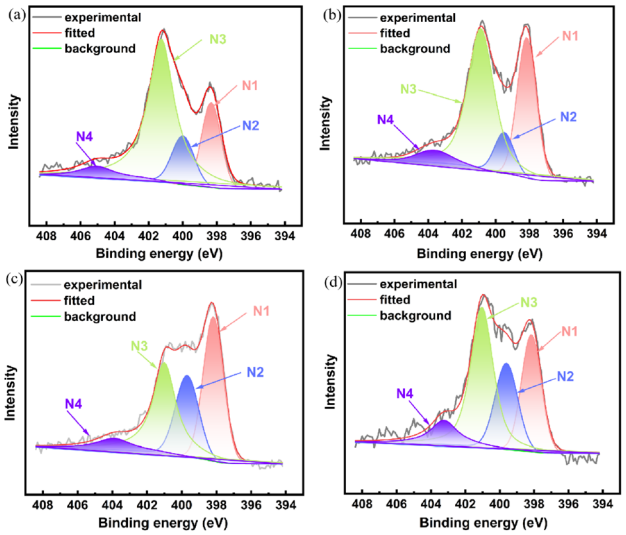

Fig. 4 XPS spectra of N 1s for (a) CNF–N, (b) CNF–N,P, (c) CNF–N,B, (d) CNF–N,P,B.

heteroatom-doped carbon nanofibers were quantified as follows: CNF–N (7.00%), CNF–N,P (10.71%), CNF–N,B (10.48%), and CNF–N,P,B (12.69%), demonstrating a positive correlation between heteroatom co-doping (P/B) and enhanced nitrogen retention efficiency during pyrolysis.

The P and B contents of the samples were investigated using XPS, with the results depicted in Fig. 5. The P 2p spectra of the P-doped samples (Fig. 5a and c) display peaks at 132.0, 133.3, and 134.0 eV, which can be attributed to P–C (P1), O–P (P2), and O=P (P3), respectively.[29] The B 1s spectra of the B-doped samples (Fig. 4b and d) show peaks at 186.7, 189.0, 192.0, and 193.8 eV, corresponding to B_4C (B1), B_3C (B2), BC_2O (B3), and BCO_2 (B4), respectively.[30] The presence of P–C and B–C bonds indicates the successful doping of P and B atoms into the

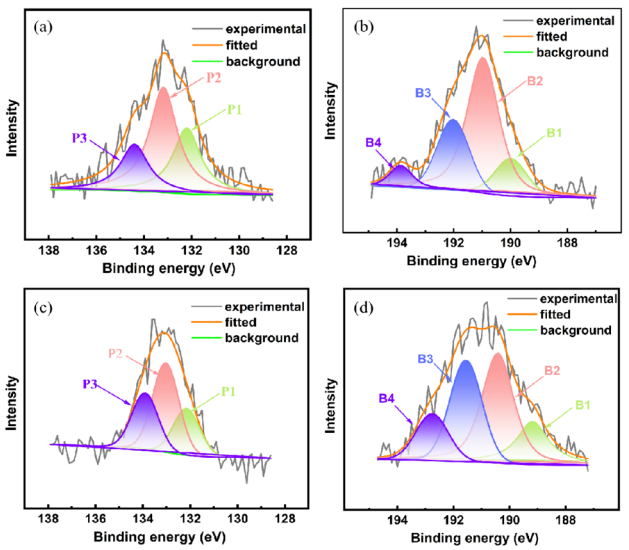

Fig. 5 XPS spectra of P 2p for (a) CNF–N,P, (c) CNF–N,P,B and B 1s for (b) CNF–N,B, (d) CNF–N,P,B.

carbon skeleton. The formation of P–C and B–C bonds in the CNFs may originate from either (i) substitutional doping *via* P and B atoms incorporation into the carbon lattice, facilitated by the atomic radius mismatch between P or B and C, or (ii) covalent edge functionalization through anchoring of P/B-containing moieties at defect sites,[27] as evidenced by the increased I_D/I_G ratio in Raman spectroscopy (from 1.01 to 1.08). It is observed that after both B and P doping, the areas of the P=O, BC_2O, and BCO_2 peaks increase significantly compared with those of single-doping samples, indicating that oxygen atoms are more involved in the bonding process for CNF–N,P,B, which may influence the electrochemical properties.[31] Moreover, the P contents in CNF–N,P and CNF–N,P,B were measured to be 0.62% and 0.82%, respectively. The B contents in CNF–N,B and CNF–N,P,B were measured to be 3.32% and 3.95%, respectively. The increased P and B contents in CNF–N,P,B could enhance the active sites and defects to boost their capacities, as well as enlarge the interlayer distances for fast Li^+ diffusion to improve their rate properties.[32]

The as-prepared CNFs were employed as binder-free electrodes in half cells to assess their Li^+ storage performance, with the results illustrated in Fig. 6. The charge–discharge curves of the third cycles for the different samples at a current density of 100 mA g^{-1} within a voltage range of 0.1–3.0 V *vs.* Li^+/Li are depicted in Fig. 5a, exhibiting slant discharge and charge plateaus around 0.5 V and 1.2 V, respectively.[16] The reversible capacities of CNF–N, CNF–N,P, CNF–N,B, and CNF–N,P,B were determined to be 370.5, 534.2, 548.2, and 595.2 mA h g^{-1}, respectively. It is evident that the capacities of CNF–N,P and CNF–N,P,B exceed that of CNF–N, with CNF–N,P,B demonstrating the highest capacity. This indicates that co-doping

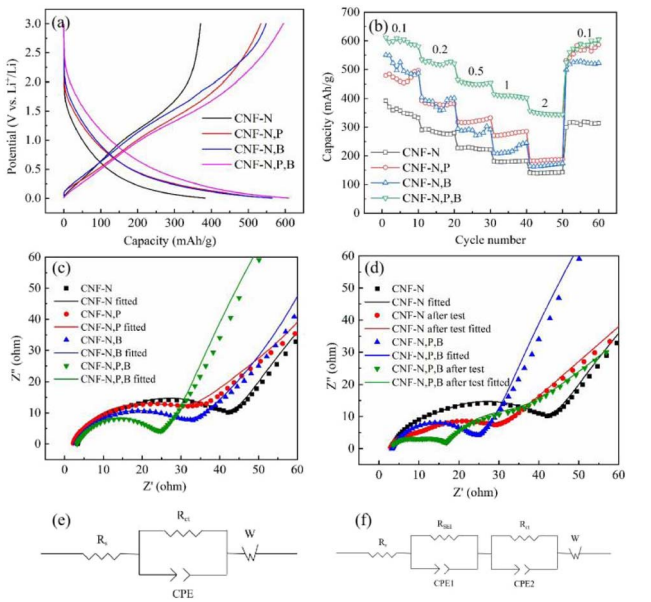

Fig. 6 (a) charge–discharge curves of the third cycles, (b) rate performance (the unit of current densities is A g^{-1}), (c) EIS curves of different samples, (d) EIS comparison before and after test for CNF–N and CNF–N,P,B (the lines are the fitted results according to the data points), the equivalent circuits of (e) before test, (f) after test.

Table 1 The comparison of our work and other carbon materials with heteroatom doping

Materials	Doping elements	Specific capacities	Reference
Carbon nanofibers	N,P,B	611.2 mA h g^{-1} at 0.1 A g^{-1}	This work
GPNx@CNTs nanofibers	N	About 300 mA h g^{-1} at 0.1 A g^{-1}	12
CNT sponges	N	290 mA h g^{-1} at 0.1 A g^{-1}	36
Graphite	F	394.9 mA h g^{-1} at 0.07 A g^{-1}	37
Graphene sheets	B	About 450 mA h g^{-1} at 0.5 A g^{-1}	38
Reduced graphene aerogel	N,P	120 mA h g^{-1} at 0.1 A g^{-1}	20
Hollow carbon fibers	N,P	310 mA h g^{-1} at 0.1 A g^{-1}	39
Carbon nanofibers	N,P	507.3 mA h g^{-1} at 0.1 A g^{-1}	19
Carbon nanofibers	N	479.44 mA h g^{-1} at 0.1 A g^{-1}	40
Carbon nanofibers	Sb_2Se_3@N-CQDs	571.4 mA h g^{-1} at 0.1 A g^{-1}	41
Carbon fibers	N	387.5 mA h g^{-1} at 0.1 A g^{-1}	42

with N, P, and B can enhance the electrochemical performance of CNF samples.[33] This finding is further corroborated by the rate properties of the different samples presented in Fig. 5b. CNF–N,P,B exhibited the highest specific capacities of 611.2, 534.1, 464.3, 414.1, and 356.3 mA h g^{-1} at current densities of 0.1, 0.2, 0.5, 1.0, and 2.0 A g^{-1}, respectively, and returned to 604.3 mA h g^{-1} when the current density was reverted to 0.1 A g^{-1}. This underscores the excellent rate performance and reversibility of CNF–N,P,B. The electrochemical properties of CNF–N,P,B were then benchmarked against those of published doped carbon anodes, as shown in Table 1, which indicates that CNF–N,P,B exhibits superior electrochemical properties.

The EIS curves of different samples are shown in Fig. 6c, where the R_{ct} of CNF–N, CNF–N,P CNF–N,B, and CNF–N,P,B were fitted to be 47.03, 40.45, 33.09, and 20.74 Ω, respectively, according to the equivalent circuit in Fig. 5e. The CNF–N,P,B exhibited the lowest R_{ct} compared with the other samples, which could be one of the reasons of its highest electrochemical properties. Furthermore, the EIS comparison of before and after 100 cycles (charged state) for CNF–N and CNF–N,P,B were measured, and the results are shown in Fig. 6d. It is observed that after 100 cycles, the sample showed two semi-circles, corresponding to the R_{SEI} and R_{ct}, respectively.[12] Based on the equivalent circuit in Fig. 5f, the R_{ct} values before and after tests were 47.03 and 48.41 Ω for CNF–N, and the values for CNF–N,P,B were 20.74 and 22.35 Ω, which indicates that the R_{ct} decreases after the cycle test, leading to excellent cycle stability.[34] In addition, the R_{SEI} of CNF–N and CNF–N,P,B were fitted to be 20.74 and 17.54 Ω, respectively, illustrating that CNF–N,P,B was less affected by the SEI film, resulting in better charge–discharge performance. However, the slope of the inclined lines decreases after test compared with the samples before test, resulting from the affect of SEI film during the discharge–charge test.[35]

Based on the preceding evaluations, the CNF–N,P,B sample exhibited superior electrochemical performance compared to other samples. Consequently, the CV curves and cycling stability of CNF–N,P,B were further investigated. Fig. 7a illustrates the CV curves of CNF–N,P,B at a scan rate of 0.5 mV s^{-1}. It is observed that the curves of the second and third cycles differ from that of the first cycle. The initial peak around 0.5 V, which is attributed to the formation of the SEI film, only appears in the first cycle and disappears in subsequent cycles. Each cycle features a discharge peak around 0.1 V and a charge peak around 0.2 V, corresponding to the insertion and extraction of Li^+, respectively. Another peak around 1.2 V is ascribed to the desorption of Li^+ from defects induced by N, P, and B doping, which significantly enhances the reversible capacity.[19,43] Additionally, the rate performance of CNF–N,P,B was assessed, with the results presented in Fig. 7b. The specific capacities were measured to be 615.3, 548.5, 445, 388, 348, 292.5, 254.3, 179.5, and 604.8 mA h g^{-1} at current densities of 0.1, 0.2, 0.5, 1, 2, 5, 10, 20, and back to 0.1 A g^{-1}, respectively. These results indicate that the successful N,P,B-triple doping endows the sample with excellent rate performance. The cycling stability of CNF–N,P,B was evaluated at a current density of 1 A g^{-1}, with the results shown in Fig. 7c. After 500 cycles, the capacity retention rate was 94.8%, demonstrating outstanding cycling stability.

In summary, the CNF–N,P,B sample, which is enhanced by P and B doping in addition to N doping, demonstrated superior electrochemical performance compared to materials doped with a single element or dual elements. This enhanced performance can be attributed to three primary factors. First, P/B co-doping introduces additional defects into the N-doped CNF, which facilitate the absorption and desorption of Li^+ ions, thereby enhancing specific capacities.[44,45] XPS analysis confirms that multi-element co-doping (N/P/B) synergistically enhances active-site density through increased pyridinic-N, pyrrolic-N, and oxygen-based groups, while higher dopant diversity amplifies total heteroatom content by 10.46%, collectively boosting capacity by 60.6% *versus* single-doped systems. This multi-element amplification effect demonstrates that diversified doping optimizes both ionic and electronic interactions, surpassing conventional binary doping limitations. Second, N/P/B co-doping synergistically enhances the material's electronic structure through complementary electron donor (P)–acceptor (B) interactions,[46] which optimize charge transfer kinetics.[47,48] The left-shifted (002) carbon peak from XRD patterns, the higher I_D/I_G value from Raman spectra, the enhanced SSA from BET curves, and the average pore diameters from pore size distribution collectively illustrate that P/B co-doping improves the N-doped CNF's defect structure. Third, EIS results indicate that R_{ct} of CNF–N,P,B is significantly reduced compared to other samples, suggesting that the defects and lattice enlargement resulting from P/B co-doping enhance electronic and ionic conductivity, leading to lower polarization

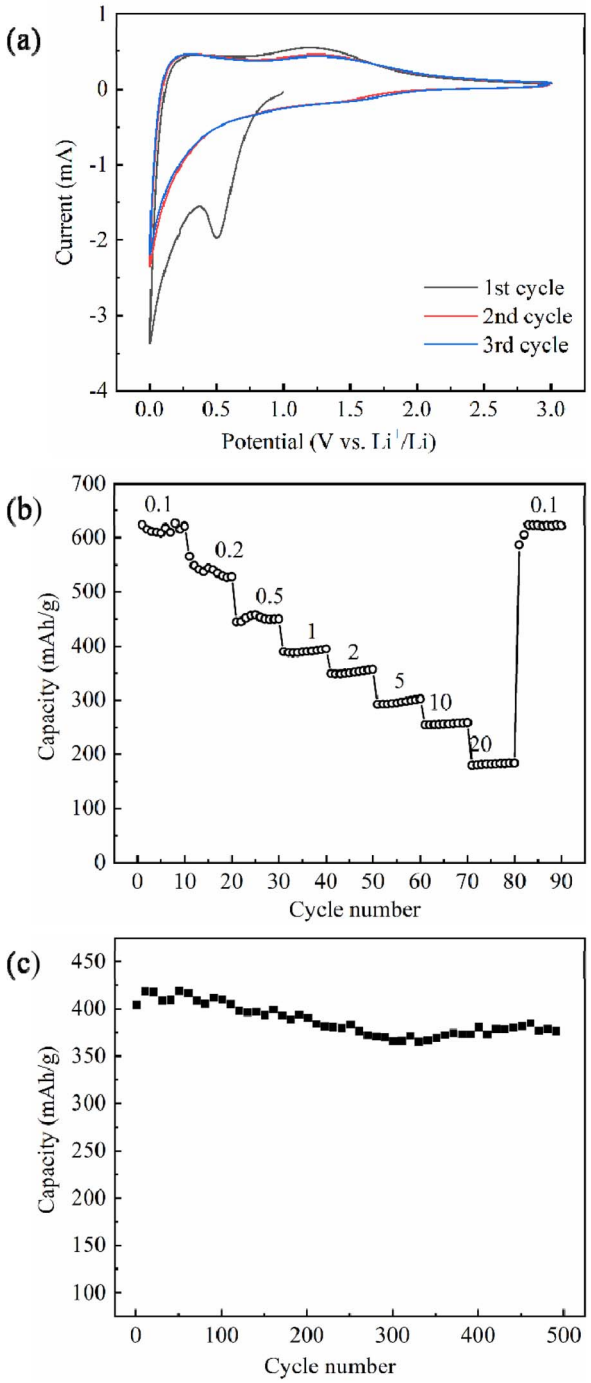

Fig. 7 (a) CV curves, (b) rate performance (the unit of current densities is A g^{-1}), and (c) cycle performance of CNF–N,P,B.

and higher capacity.[49,50] Collectively, these factors contribute to the improved electrochemical properties of CNF–N,P,B for LIC applications.

Conclusions

This study developed P and B enhanced N-doped carbon nanofibers through electrospinning as binder-free anodes for lithium-ion storage application. Compared to single-element-doped analogs (CNF–N, CNF–N,P, CNF–N,B), the CNF–N,P,B exhibited enriched structural defects and electrochemically active sites, resulting in an elevated specific surface area (252.00 m^2 g^{-1}) and optimized charge transfer kinetics. These synergistic effects from multi-heteroatom co-doping endowed the CNF–N,P,B with exceptional lithium storage performance: a high reversible capacity of 611.2 mA h g^{-1} at 0.1 A g^{-1}, remarkable rate capability (179.5 mA h g^{-1} at 20 A g^{-1}), and robust cyclability (94.8% capacity retention after 500 cycles). The work demonstrates an innovative and scalable approach to designing high-performance carbonaceous anodes *via* strategic multi-element doping and binder-free architecture engineering.

Data availability

All data generated or analyzed during this study are included in this published article.

Conflicts of interest

There are no conflicts to declare.

Acknowledgements

This research was funded by Sichuan Province Science and Technology Support Program (Grant No. 2023NSFSC0870), National Natural Science Foundation of Hunan (2025JJ50065), and Opening Foundation of Sichuan Province Engineering Research Center for Urban Solid Waste Energy and Building Material Conversion Technology, Chengdu University (GF2024YB03).

References

1 M. Li, S. Song, Y. Li, W. Jevasuwan, N. Fukata and J. Bae, Binder-free boron-doped Si nanowires toward the enhancement of lithium-ion capacitor, *Nanotechnology*, 2023, **34**, 355401.
2 P. Smith, T. Tran, T. Liang and J. Chung, Lithium-ion capacitors: electrochemical performance and thermal behavior, *J. Power Sources*, 2013, **243**, 982–992.
3 H. Wang, C. Zhu, D. Chao, Q. Yan and H. Fan, Nonaqueous hybrid lithium-ion and sodium-ion capacitors, *Adv. Mater.*, 2017, **29**, 1702093.
4 Y. Liu, W. Wang, J. Chen, X. Li, Q. Cheng and G. Wang, Fabrication of porous lithium titanate self-supporting anode for high performance lithium-ion capacitor, *J. Power Sources*, 2020, **50**, 344–350.
5 C. Han, H. Li, R. Shi, L. Xu, J. Li, F. Kang and B. Li, Nanostructured anode materials for non-aqueous lithium ion hybrid capacitors, *Energy Environ. Mater.*, 2018, **1**, 75–87.
6 S. Zhao, X. Zhang, C. Li, Y. An, T. Hu, K. Wang, X. Sun and Y. Ma, The application of metal-organic frameworks and their derivatives for lithium-ion capacitors, *New Carbon Mater.*, 2024, **39**(5), 872–895.
7 G. Wang, C. Lu, X. Zhang, B. Wan, H. Liu, M. Xia, H. Gou, G. Xin, J. Lian and Y. Zhang, Toward ultrafast lithium ion

capacitors: a novel atomic layer deposition seeded preparation of $Li_4Ti_5O_{12}$/graphene anode, *Nano Energy*, 2017, **36**, 46–57.

8 J. Jiang, Q. Shen, Z. Chen and S. Wang, Nitrogen-doped porous carbon derived from coal for high-performance dual-carbon lithium-ion capacitors, *Nanomaterials*, 2023, **13**, 2525.

9 B. Chen, Z. Qi, B. Chen, X. Liu, H. Li, X. Han, G. Zhou, W. Hu, N. Zhao and C. He, Room-Temperature Salt Template Synthesis of Nitrogen-Doped 3D Porous Carbon for Fast Metal-Ion Storage, *Angew. Chem., Int. Ed.*, 2024, **63**(1), e202316116.

10 U. Bhattacharjee, M. Bhar, S. Ghosh, S. Bhowmik and S. Martha, A dual carbon lithium-ion capacitor using recycled polymer separator derived carbon cathode and graphite anode from spent lithium-ion battery, *J. Electrochem. Soc.*, 2023, **170**, 090533.

11 M. Wang, Y. Zhu, Y. Chen, S. Zhao, G. Li, Z. Yu, W. Ning, J. Liu and X. Wang, Lignin-derived honeycomb-like porous carbon for high-performance lithium-ion battery anodes, *Diamond Relat. Mater.*, 2025, **155**, 112297.

12 S. Hu, Z. Ge, J. Tan, H. Lai, T. Feng, S. Zhang, Z. Xu, H. Zhou, X. Cao, G. Zhu and M. Wu, Dual-functionally modified N/S doped hierarchical porous carbon and glycerol-engineered polyacrylonitrile carbon nanofibers combine for high-performance lithium-ion capacitors, *J. Power Sources*, 2023, **558**, 232624.

13 K. Sung, K. Ko and H. Ahn, Tailored sulfur and nitrogen co-doped carbon quantum dot interfacial layer on copper foil for highly stable and ultrafast lithium-ion capacitors, *J. Energy Storage*, 2023, **72**, 108797.

14 Y. Zhong, H. Xiong, J. Low, R. Long and Y. Xiong, Recent progress in electrochemical C-N coupling reactions, *eScience*, 2023, **3**, 100086.

15 F. Yang, P. Jiang, Q. Wu, W. Dong, M. Xue and Q. Zhang, Preparation and Lithium-Ion Capacitance Performance of Nitrogen and Sulfur Co-Doped Carbon Nanosheets with Limited Space *via* the Vermiculite Template Method, *Molecules*, 2024, **29**, 536.

16 M. Chen, T. Le, Y. Zhou, F. Kang and Y. Yang, Enhanced electrode matching assisted by *in situ* etching and co-doping toward high-rate dual-carbon lithium-ion capacitors, *ACS Sustainable Chem. Eng.*, 2021, **9**, 10054–10061.

17 F. Yu, Z. Liu, R. Zhou, D. Tan, H. Wang and F. Wang, Pseudocapacitance contribution in boron-doped graphite sheets for anion storage enables high-performance sodium-ion capacitors, *Mater. Horiz.*, 2018, **5**, 529–535.

18 T. Li, J. Zhang, C. Li, H. Zhao, J. Zhang, Z. Qian, L. Yin and R. Wang, Nitrogen and phosphorous co-doped hierarchical meso-microporous carbon nanospheres with extraordinary lithium storage for high-performance lithium-ion capacitors, *Sci. China Mater.*, 2022, **65**, 2363–2372.

19 C. Yang, M. Zhang, N. Kong, J. Lan, Y. Yu and X. Yang, Self-supported carbon nanofiber films with high-level nitrogen and phosphorus co-doping for advanced lithium-ion and sodium-ion capacitors, *ACS Sustainable Chem. Eng.*, 2019, **7**, 9291–9300.

20 S. Alomari, D. Dubal, J. MacLeod, S. Jadhav, C. Padwal and N. Motta, Nitrogen, phosphorus co-doped holey rGO as a cathode material for Li-ion capacitors, *Appl. Surf. Sci.*, 2023, **641**, 158452.

21 J. Lin, Y. Shi, Y. Li, Y. Song, X. Wu and H. Sun, B/N/O-codoped 2D porous carbon nanosheets for high-performance dual-carbon lithium-ion capacitors, *ACS Appl. Energy Mater.*, 2023, **6**(17), 8867–8874.

22 M. Shi, D. Bao, S. Li, B. Wulan, J. Yan and Q. Jiang, Anchoring PdCu amorphous nanocluster on graphene for electrochemical reduction of N_2 to NH_3 under ambient conditions in aqueous solution, *Adv. Energy Mater.*, 2018, **8**, 1800124.

23 Z. Sun, H. Liu, W. Li, N. Zhang, S. Zhu, B. Chen, F. He, N. Zhao and C. He, Advanced hard carbon materials for practical applications of sodium-ion batteries developed by combined experimental, computational, and data analysis approaches, *Prog. Mater. Sci.*, 2025, **149**, 101401.

24 H. Huang, R. Xu, Y. Feng, S. Zeng, Y. Jiang, H. Wang, W. Luo and Y. Yu, Sodium/potassium-ion batteries: boosting the rate capability and cycle life by combining morphology, defect and structure engineering, *Adv. Mater.*, 2020, **32**, 1904320.

25 Z. Pei, J. Gu, Y. Wang, Z. Tang, Z. Liu, Y. Huang, Y. Huang, J. Zhao, Z. Chen and C. Zhi, Component matters: paving the roadmap toward enhanced electrocatalytic performance of graphitic C_3N_4-based catalysts *via* atomic tuning, *ACS Nano*, 2017, **11**, 6004–6014.

26 S. Ghosh, S. Barg, S. Jeong and K. Ostrikov, Heteroatom-doped and oxygen-functionalized nanocarbons for high-performance supercapacitors, *Adv. Energy Mater.*, 2020, **10**, 2001239.

27 N. Gupta and P. Bhattacharya, Microwave-plasma induced one-step synthesis of $Ni(PO_3)_2$ nanosphere-loaded bio-waste derived N, P co-doped carbon for an asymmetric supercapacitor with prolonged life, *J. Mater. Chem. C*, 2023, **11**, 13503.

28 A. S. R. Choudhury, S. Kumar, N. Gupta, A. Jana and P. Bhattacharya, Mechanochemically assisted microwave-induced plasma synthesis of a N-doped graphitic porous carbon-based aqueous symmetric Supercapacitor with ultrahigh volumetric capacitance and energy density, *ACS Appl. Electron. Mater.*, 2024, **6**, 1140–1150.

29 Z. Li, Z. Xu, H. Wang, J. Ding, B. Zahiri, C. Holt, X. Tan and D. Mitlin, Colossal pseudocapacitance in a high functionality-high surface area carbon anode doubles the energy of an asymmetric supercapacitor, *Energy Environ. Sci.*, 2014, **7**, 1708–1718.

30 X. Yan, Y. Liu, X. Fan, X. Jia, Y. Yu and X. Yang, Nitrogen/phosphorus co-doped nonporous carbon nanofibers for high-performance supercapacitors, *J. Power Sources*, 2014, **248**, 745–751.

31 Z. Wu, W. Ren, L. Xu, F. Li and H. Cheng, Doped graphene sheets as anode materials with superhigh rate and large

capacity for lithium ion batteries, *ACS Nano*, 2011, **5**, 5463–5471.

32 J. Lin, Y. Shi, Y. Li, Y. Song, X. Wu and H. Sun, B/N/O-codoped 2D porous carbon nanosheets for high performance dual-carbon lithium-ion capacitors, *ACS Appl. Energy Mater.*, 2023, **6**, 8867–8874.

33 H. Tao, L. Xiong, S. Du, Y. Zhang, X. Yang and L. Zhang, Interwoven N and P dual-doped hollow carbon fibers/graphitic carbon nitride: an ultrahigh capacity and rate anode for Li and Na ion batteries, *Carbon*, 2017, **122**, 54–63.

34 W. Zhao, J. Yang, B. Yang, Z. Gao, D. Han, Q. Su, B. Xu and G. Du, N-doped carbon knotting carbon nanotube sponge networks for lithium-ion capacitor anodes, *ACS Appl. Nano Mater.*, 2023, **6**, 9306–9314.

35 Q. Li, L. Li, P. Wu, N. Xu, L. Wang, M. Li, A. Dai, K. Amine, L. Mai and J. Lu, Silica restricting the sulfur volatilization of nickel sulfide for high-performance lithium-ion batteries, *Adv. Energy Mater.*, 2019, **9**, 1901153.

36 C. Ma, X. Shao and D. Cao, Nitrogen-doped graphene nanosheets as anode materials for lithium ion batteries: a first-principles study, *J. Mater. Chem.*, 2012, **22**, 8911.

37 W. Zhao, J. Yang, B. Yang, Z. Gao, D. Han, Q. Su, B. Xu and G. Du, N-doped carbon knotting carbon nanotube sponge networks for lithium-ion capacitor anodes, *ACS Appl. Nano Mater.*, 2023, **6**(11), 9306–9314.

38 J. Youn, G. Park, M. Kim, S. Kang, D. Jang and W. Kim, Surface modification with F-doped carbon layer coating on natural graphite anode for improving interface compatibility and electrochemical performance of lithium-ion capacitors, *ACS Appl. Electron. Mater.*, 2023, **5**(8), 4344–4353.

39 U. Bhattacharjee, S. Bhowmik, S. Ghosh, N. Vangapally and S. Martha, Boron-doped graphene anode coupled with microporous activated carbon cathode for lithium-ion ultracapacitors, *Chem. Eng. J.*, 2022, **430**, 132835.

40 H. Xu, Z. Peng, Y. Yang, C. Yin, X. Li, H. Liu, S. Li, Y. Luo and L. Zhou, Nitrogen-Doped Carbon Nanofibers as Free-Standing and Binder-Free Anode Materials for Lithium-Ion Batteries, *ACS Appl. Nano Mater.*, 2025, **8**(17), 9004–9015.

41 C.-H. Wu, S. Kubendhiran, R.-J. Chung, C. Kongvarhodom, S. Husain, S. Yougbard, H.-M. Chen, Y.-F. Wu and L.-Y. Lin, Hierarchical design of carbon nanofibers wrapped antimony selenide nanorods with heteroatom-doped carbon quantum dots as efficient anode material of high-performance sodium-ion batteries, *J. Power Sources*, 2024, **623**, 235469.

42 X. Han, H. Guo, B. Xing, H. Liang, H. Zeng, W. Kang, X. Qu, C. Zhang, Y. Cao and Z. Chen, A facile electrospinning strategy to prepare cost-effective carbon fibers as a self-supporting anode for lithium-ion batteries, *Fuel*, 2024, **373**, 132277.

43 Y. Zhou, S. Tian, M. Jia, P. Gao, G. Yin, X. Wang, J. Mu, J. Zhou and T. Zhou, Phosphorus/nitrogen co-doped hollow carbon fibers enabling high-rate potassium storage, *Rare Met*, 2023, **42**, 2622–2632.

44 X. Liu, J. Zhang, S. Guo and N. Pinna, Graphene/N-doped carbon sandwiched nanosheets with ultrahigh nitrogen doping for boosting lithium-ion batteries, *J. Mater. Chem. A*, 2016, **4**, 1423–1431.

45 Y. Zhou, S. Tian, M. Jia, P. Gao, G. Yin, X. Wang, J. Mu, J. Zhou and T. Zhou, Phosphorus/nitrogen co-doped hollow carbon fibers enabling high-rate potassium storage, *Rare Met*, 2023, **42**(8), 2622–2632.

46 C. Cheng, J. Yu, D. Xu, L. Wang, G. Liang, L. Zhang and M. Jaroniec, In-situ formatting donor-acceptor polymer with giant dipole moment and ultrafast exciton separation, *Nat. Commun.*, 2024, **15**, 1313.

47 W. Sun, Q. Sun, R. Lu, M. Wen, C. Liu, J. Xu and Y. Wu, Sodium hypophosphite-assist pyrolysis of coal pitch to synthesis P-doped carbon nanosheet anode for ultrafast and long-term cycling sodium-ion batteries, *J. Alloys Compd.*, 2021, **889**, 161678.

48 J. Yu, C. Ding, X. Wang and P. Huang, Optimized synthesis of N-doped multi-channel carbon derived from fiber-reinforced polyimide composites for supercapacitors, *Mater. Lett.*, 2023, **339**, 134036.

49 M. Wu, X. Hu, W. Zheng, L. Chen and Q. Zhang, Recent advances in porous carbon nanosheets for high-performance metal-ion capacitors, *Chem. Eng. J.*, 2023, **466**(15), 143077.

50 K. Sung, K. Ko and H. Ahn, Tailored sulfur and nitrogen co-doped carbon quantum dot interfacial layer on copper foil for highly stable and ultrafast lithium-ion capacitors, *J. Energy Storage*, 2023, **72**, 108797.